



NIR-II fluorescence nanoprobe based on Erbium for fallopian tube diseases diagnosis



Guangxin Duan^{b,1}, Zhuxin Wei^{a,1}, Jingyu Zhang^c, Xuexiao Li^b, Shuwang Wu^b, Jianfeng Zeng^b, Ximing Wang^a, Hong Zhang^{d,*}, Ling Wen^{a,**}, Mingyuan Gao^b

^a Department of Radiology, The First Affiliated Hospital of Soochow University, Institute of Medical Imaging, Soochow University, 188 Shizi Street, Suzhou, Jiangsu 215000, China

^b State Key Laboratory of Radiation Medicine and Protection, School for Radiological and Interdisciplinary Sciences (RAD-X), Collaborative Innovation Center of Radiation Medicine of Jiangsu Higher Education Institutions, Soochow University, 199 Renai Road, Suzhou, Jiangsu 215123, China

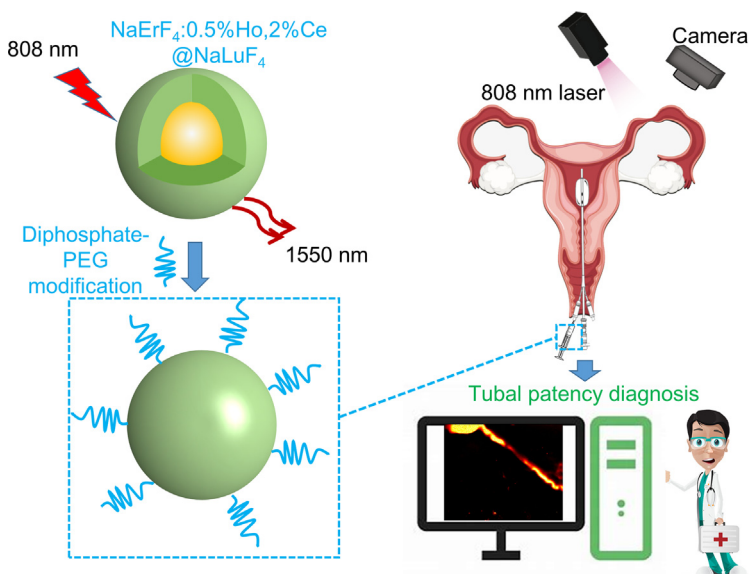
^c Department of Surgery, the Second Affiliated Hospital of Soochow University, Suzhou 215004, China

^d Department of Obstetrics and Gynecology, The Second Affiliated Hospital of Soochow University, Suzhou 215004, China

HIGHLIGHTS

- A well-performance NIR-II fluorescence nanoprobe (Er-RENPs), which emission at 1550 nm with 808 nm laser excitation, is fabricated by simple one-pot reaction.
- NIR-II imaging can clearly visualize the structure of fallopian tubes, as well as accurately diagnose common fallopian tubal diseases with the aid of Er-RENPs nanoprobe.
- The Er-RENPs can be excreted into abdominal cavity in 120 min after administration, and exhibit good biocompatibility.
- NIR-II imaging has the potential to be an alternative to HSG for tubal patency diagnosis, with the aid of Er-RENPs nanoprobe.

GRAPHICAL ABSTRACT



ARTICLE INFO

Article history:

Received 11 October 2022

Revised 17 January 2023

Accepted 10 February 2023

Available online 13 February 2023

Keywords:

Erbium-based rare-earth nanoparticles

ABSTRACT

Fallopian tube blockage-related diseases are the main cause of female infertility. Diagnosis of tubal patency and accurate determination of tubal obstruction lesions is of great value for infertility treatment. Conventionally, the common used hysterosalpingogram (HSG) has the disadvantages of radioactive hazard and high false positive rate. Thus, the development of a safe and accurate method which can replace traditional HSG for tubal patency diagnosis is urgently needed. Recently, fluorescence imaging in the second near-infrared region (NIR-II) was widely used in *in-vivo* imaging research due to its excellent tissue penetration and signal-to-noise ratio. With the aid of fluorescence agents, NIR-II imaging has the potential to diagnose tubal patency, which, unfortunately, has not been explored. Herein, a kind of rare-earth

* Corresponding author.

** Corresponding author.

E-mail addresses: szhanghong126@126.com (H. Zhang), wenling@suda.edu.cn (L. Wen).

¹ Equal contribution.

NIR-II fluorescence
Fallopian tube imaging
Fallopian tube diseases diagnosis

Erbium-based nanoprobe (Er-RENPs) with outstanding NIR-II fluorescence property was synthesized. Based on the Er-RENPs, the potential of NIR-II fluorescence imaging was explored. Results show that the outline of fallopian tubes can be clearly visualized with the help of Er-RENPs. And the stenotic, occlusive fallopian tubes and hydrosalpinx can be diagnosed. Additionally, the Er-RENPs exhibit good biocompatibility. In this study, we reported that NIR-II rare-earth fluorescent nanoprobe can serve as a promising fluorescent agent, and exhibits considerable potential application for tubal diagnosis.

© 2023 The Authors. Published by Elsevier Ltd. This is an open access article under the CC BY-NC-ND license (<http://creativecommons.org/licenses/by-nc-nd/4.0/>).

1. Introduction

The fallopian tube is an elongated and curved tube connecting the uterus and ovary. It is an important part of the female reproductive system where fertilization takes place as well as embryos are nourished at the early stage [1]. Tubal diseases caused by pelvic infection, pelvic adhesion, ovarian surgery, endometriosis and congenital anomaly may lead to partial blockage and even complete occlusion of fallopian tube *i.e.* poor tubal patency, which hinders fertilization between sperm and oocyte, further resulting in infertility [2]. Statistically, poor tubal patency accounts for appropriately one-third of female infertility [3]. Almost all female infertility patients should be checked for tubal patency. Hence, accurate diagnosis of tubal patency is significant for recanalization, and the other infertility treatments.

Clinically, hydrotubation, hysterosalpingogram (HSG) are usually performed to investigate the tubal patency [4–6]. Hydrotubation refers injecting sterilized isotonic saline solution or the other dye solution into fallopian tube, and the injection resistance and reflux fluid volume are analyzed to evaluate the patency [7]. The diagnosis has the advantage of being simple and inexpensive. However, it also has obvious shortcomings, such as the inability to visualize the fallopian tubes and determine the location of blockage [8]. In contrast, HSG which by means of X-ray imaging and iodinated media as contrast agents, is specialized in visualizing the internal architecture of the fallopian tubes, and pinpointing the blockage lesions. Thus, it is considered to be the gold standard to diagnose tubal patency, and more commonly used clinically [9]. Unfortunately, HSG not only causes great uncomfortable to the patients, but also puts patients at risk of radiation [10]. Even worse is that the iodinated contrast agents utilized in HSG may lead to tubal spasm in the corneal region, which may be misdiagnosed as proximal tubal obstruction. Previous study has shown that as much as 62% of patients who diagnosed with tubal occlusion by HSG actually have open fallopian tubes [11]. Therefore, it is of great importance to develop a novel accurate diagnosis strategy for fallopian tubal diseases.

Fluorescence imaging is a common imaging modality, which is widely used in medical and molecular biology imaging [12,13], due to its high sensitivity and biosafety. Limited by the shortcomings of penetration and signal-to-noise ratio (SNR), however, tradition fluorescence imaging is rarely applied to *in vivo* imaging. With the rapid development of fluorescence imaging technology in recent years, fluorescence imaging in the second near-infrared region (NIR-II, 1000–1700 nm) has attracted extensive attention on account of its excellent penetration and ultra-high SNR [14–17]. On that account, NIR-II fluorescence imaging is extensively utilized in *in vivo* tumor imaging [18,19], blood vessel imaging [20,21], lymphatic system imaging [22–24], inflammatory lesion imaging [25–27]. Of note, NIR-II fluorescence imaging was reported successfully used in human liver tumor surgery for providing fluorescent navigation, which illustrates the great potential of NIR-II imaging in clinical diagnosis [28]. Based on above, NIR-II imaging has great potential for replacing HSG to achieve accurate,

radiation-free diagnosis of tubal patency, which, unfortunately, have not been and reported so far.

To evaluate the application value of NIR-II imaging in the tubal diagnosis, the selection of well-performance NIR-II probe is essential. The well-studied NIR-II probes include carbon nanotubes (CNTs) [29], quantum dots (QDs, such as AgS QDs [30], AgSe QDs [31]), organic NIR-II probes (such as modified ICG [28], aggregation-induced emission luminogen dots [32]), and rare-earth nanoparticles [33]. Thanks to their excellent fluorescent properties and good biocompatibility, rare-earth nanoparticles have attracted extensive attention, and have been widely investigated. Based on the obvious advantages, rare-earth nanoparticles may be ideal NIR-II fluorescent agents for precise tubal patency diagnosis. Herein, the rare-earth Erbium-based $\text{NaErF}_4\cdot 0.5\% \text{Ho}_2\text{O}_3\cdot 2\% \text{Ce}@ \text{NaLuF}_4$ nanoparticles (Er-RENPs) whose emitting peak located at 1550 nm were synthesized. Further, the NIR-II nanoprobe exhibited high-performance diagnostic of rabbit tubal diseases such as complete tubal occlusion, mild tubal obstruction, and tubal breakage. Additionally, almost all of the NIR-II nanoprobe can flow into abdominal cavity from fallopian tubes in 120 min, and exhibits excellent *in vivo* biocompatibility. Our study confirmed the potential of NIR-II imaging as an alternative to HSG for tubal patency diagnostics, as well as the prospect of Er-RENPs for tubal diagnosis.

2. Experimental section

2.1. Materials and reagents

Erbium (III) chloride hexahydrate ($\text{ErCl}_3\cdot 6\text{H}_2\text{O}$, 99.9%), lutetium (III) chloride hexahydrate ($\text{LuCl}_3\cdot 6\text{H}_2\text{O}$, 99.99%), holmium (III) chloride hexahydrate ($\text{HoCl}_3\cdot 6\text{H}_2\text{O}$, 99.9%), cerium (III) chloride hexahydrate ($\text{CeCl}_3\cdot 6\text{H}_2\text{O}$, 99.9%), sodium fluoride (NaF, 99.99%), Sodium hydroxide (NaOH, 96%), 1-octadecene (ODE, 90%) and oleic acid (OA, 85%) were obtained from Aladdin Co. Ltd. (Shanghai, China). Analytical grade tetrahydrofuran (THF) was purchased from Shanghai Titan Scientific Co. Ltd. (Shanghai, China). PEG-2000 modified with diphosphate group and methoxy group on the two ends ($\text{CH}_3\text{O}-\text{PEG}-\text{DP}$, Mw: 2000) respectively were customized products provided by Beijing Oneder Hightech Co. Ltd. (Beijing, China). CCK-8 reagent was purchased from Dojindo Laboratories (Kumamoto, Japan). Fetal bovine serum (FBS) and Penicilium-Streptomycin (Penicilium 100 U/mL and Streptomycin 100 $\mu\text{g}/\text{mL}$) were purchased from Gibco Life Technologies Co. Ltd. (Grand Island, USA). Dulbecco's Modified Eagle Medium (DMEM) was obtained from BasalMedia Technologies Co. Ltd.

2.2. Synthesis and characterization of Er-RENPs

The Er-RENPs were synthesized according to the simple one-pot reaction we have reported [34]. Firstly, the ultra-small lanthanide fluoride nanocluster precursors were prepared referring to liquid–solid–solution (LSS) strategy [35]. As for the shell precursor synthesis, 1 mL of Lutetium (III) chloride hexahydrate aqueous-

lution (0.5 mol/L) together with 4 mL of sodium fluoride solution (0.5 mol/L) were added drop by drop to a mixture including sodium hydroxide (1.2 g), ethanol (8 mL), deionized water (4 mL), and oleic acid (20 mL). The prepared mixture solution was stirred at room temperature for 1 h, and then precipitated with ethanol to collect NaLuF₄ nanoclusters. After being washed with ethanol for several times, the NaLuF₄ nanoclusters were dispersed in cyclohexane (2 mL) for further use. Following the similar process, the core Er/Ho/Ce (97.5% Er, 0.5% Ho, 2% Ce) precursor was fabricated. Subsequently, 2 mL of NaErF₄:0.5%Ho, 2%Ce nanoclusters solution (0.5 mmol) was mixed with OA (6 mL) and ODE (10 mL). The mixture was purged with nitrogen (N₂) at 70 °C for 30 min to fully remove the cyclohexane, and then heated up to 280 °C at a rate of ~10 °C/min in a flask. After reaction for 30 min at 280 °C, and cooling to 70 °C, the reaction mixture was added with 2 mL of NaLuF₄ nanoclusters solution (0.5 mmol), 6 mL of OA, and 10 mL of ODE. The resultant solution was maintained at 70 °C for 30 min, and heated up to 280 °C to maintain the reaction for 60 min to fabricate NaErF₄:0.5%Ho,2%Ce@NaLuF₄ nanoparticles. The core-shell nanoparticles were collected by centrifugation, purified by washing with ethanol, and dispersed in cyclohexane for further experiments. As for PEG modification, after 100 mg of PEG-diphosphate ligand (DP-PEG₂₀₀₀), 10 mg OA-coated NaErF₄:0.5%Ho,2%Ce@NaLuF₄ core-shell nanoparticles added into 5 mL of THF, the ligand exchange was performed under the condition of stirring for 24 h at 40 °C. Following precipitated with cyclohexane, and dried in a vacuum at room temperature, the nanoparticles were dispersed in Milli-Q water, and purified by ultrafiltration three times to remove free-polymer.

Appropriate volumes of water-soluble PEGylated Er-RENPs were taken and dropped on the copper mesh. Following drying, the morphology of the Er-RENPs was detected and recorded through TEM (FEI Tecnai G20, USA) with the parameter of acceleration voltage of 200 kV. Subsequently, Nano Measurer 1.2 software was utilized to analyze the distribution of the nanoparticles. Hydrodynamic diameter of PEGylated Er-RENPs was measured by Zetasizer Nano ZS90 dynamic light scattering (DLS, Malvern, UK) at 1, 24 and 48 h respectively. The fluorescence spectrum of OA-modified Er-RENPs was recorded by FLS980 spectra (Edinburgh Instruments, UK) operating with the parameters of 1 W 808 nm laser excitation, and slit width 3 nm.

2.3. Cytotoxicity evaluation of PEGylated Er-RENPs

The classical CCK-8 assay was performed here to investigate the cytotoxicity induced by Er-RENPs. Rapidly proliferating HeLa and NIH 3T3 cells cultured in complete DMEM medium (containing 10% FBS and 1% Penicillin-Streptomycin) were collected after digestion, and plated into 96-well plates in the concentration of 5000 cells/well. Following incubation in incubator (37°C, 5% CO₂) for 24 h, cells were dosed with 0, 25, 50, 100, 200, 400, and 600 µg mL⁻¹ Er-RENPs (quantified with concentration of Er), and incubated for another 24 h in incubator. Then, media containing Er-RENPs were abandoned, and fresh media containing 10% CCK-8 reagent were added into 96-well plates. After incubation for 2 h, absorbance at 450 nm was measured by EnSpire® Multimode Plate Reader (PerkinElmer, USA). Cell viability was calculated according to the following equation:

$$\text{Cell viability} = (A_{\text{sample}} - A_{\text{blank}}) / (A_{\text{control}} - A_{\text{blank}}) \times 100\%.$$

2.4. Photostability and fidelity of Er-RENPs

Er-RENPs (0.2 mg/mL) and ICG (0.02 mg/mL) solutions were exposed to 808 nm laser at the power density of 1 W/cm². Images of Er-RENPs and ICG tubes were taken every 5 min after laser

irradiation by NIR-II Imaging System (Yingrui optics, China). Finally, photostability was analyzed by measure mean fluorescent pixel intensity. For fidelity analysis, firstly, Er-RENPs (1 mg/mL) and ICG (0.1 mg/mL) solutions were injected into capillaries. Then, capillary fluorescence images of Er-RENPs and ICG were recorded by NIR-II Imaging System with using LP1250 and LP880 filters, respectively. Phantom width of Er-RENPs and ICG capillary images was analyzed by ImageJ software.

2.5. Animal experiments

The female New Zealand rabbits used in the research were obtained from Laboratory Animal Center of Soochow University. All of the animal experiments were performed according to protocols approved by the Institutional Animal Care and Use Committee of Soochow University.

2.6. NIR-II fluorescence imaging of normal and slender fallopian tubes using Er-RENPs

Firstly, healthy female New Zealand rabbits weighting about 3 kg were anesthetized with 10% chloral hydrate at the dose of 2 mL kg⁻¹. After the processes of fixing, shaving, and sterilizing carried out, the rabbits were operated with laparotomy, and shown both sides of the uterus. A catheter was placed into fallopian tube at the utero-tubal junction. Then, 400 µL of PEGylated Er-RENPs (1 mg mL⁻¹) were injected into fallopian tube. Immediately after Er-RENPs injection, Real-time NIR-II imaging was implemented by the NIR-II Imaging System (Serious II 900-1700) equipping the long-pass filter of 1250 nm, and operating with the parameter of 5 W 808 nm laser excitation, exposure time 200 ms. The New Zealand rabbits weighting about 1.5 kg were selected to detect slender fallopian tubes by using NIR-II imaging.

2.7. NIR-II fluorescence imaging of tubal occlusion and stenosis using Er-RENPs

3 kg female New Zealand rabbits were selected to construct tubal stenosis and occlusion models. After anesthesia, disinfection, and laparotomy, fallopian tube was ligated tightly with sterile surgical suture at the place 2 cm from the utero-tubal junction. As for the tubal stenosis model, a stent 2 cm in length, and 3 mm in diameter was placed parallel to the fallopian. Thereafter, fallopian tube and stent were ligated together with sterile surgical suture at the place 2 cm from the utero-tubal junction. Finally, the stent was pulled out gently to establish the tubal stenosis model. After modeling, 400 µL of PEGylated Er-RENPs (1 mg mL⁻¹) were injected into fallopian tubes, and modeling fallopian tubes were imaging by NIR-II Imaging System.

2.8. NIR-II fluorescence imaging of fallopian tube with hydrosalpinx using Er-RENPs

The female New Zealand rabbits weighting 3 kg were selected, and subjected to anesthesia, disinfection, and laparotomy as described above. Appropriate volume of isotonic saline solution was injected into fimbriae tubae uterinae to construct hydrosalpinx model. Thereafter, 400 µL of PEGylated Er-RENPs (1 mg mL⁻¹) were injected into fallopian tube at utero-tubal junction. And fallopian tube with hydrosalpinx was imaged using NIR-II Imaging System. Hydrosalpinx was treated by placing a stent (Bard) into the fallopian tube to the tubal fimbria. After treatment, the Er-RENPs were injected again to determine the patency of fallopian tubes by NIR-II imaging.

2.9. NIR-II fluorescence imaging the process of Er-RENPs excretion from fallopian tube

The process of Er-RENPs excretion from fallopian tubes was monitored in normal and stenotic fallopian tubes. The stenotic fallopian tube model was constructed as described above. Immediately after 400 μL of PEGylated Er-RENPs (1 mg mL^{-1}) injection into normal or stenotic fallopian tubes, NIR-II imaging was recorded by NIR-II Imaging System.

2.10. Histological analysis

To investigate the *in vivo* biocompatibility, normal female New Zealand rabbits weighting 3 kg were injected with 400 μL of sterilized isotonic saline solution (control group) and 400 μL of PEGylated Er-RENPs (1 mg mL^{-1}) to fallopian tubes, respectively. After

imaging for 2 h, rabbits were sacrificed and dissected. Fallopian tubes, uterus, ovaries were removed, and fixed in 4% paraformaldehyde solution overnight at room temperature. Thereafter, fixed samples were embedded with paraffin, sectioned into thin slices, and staining with hematoxylin and eosin (H&E). Finally, histological sections were observed by Leica optical microscope (DMI8), and photographed through Las X software.

3. Results and discussion

We synthesized Er-RENPs according to the strategy reported by our group previously [34]. The morphology and size of the Er-RENPs were observed by transmission electron microscopy (TEM). As shown in Fig. 1a, the well-prepared Er-RENPs displayed the uniform spherical shape with an average size of $13.4 \pm 1.1 \text{ nm}$,

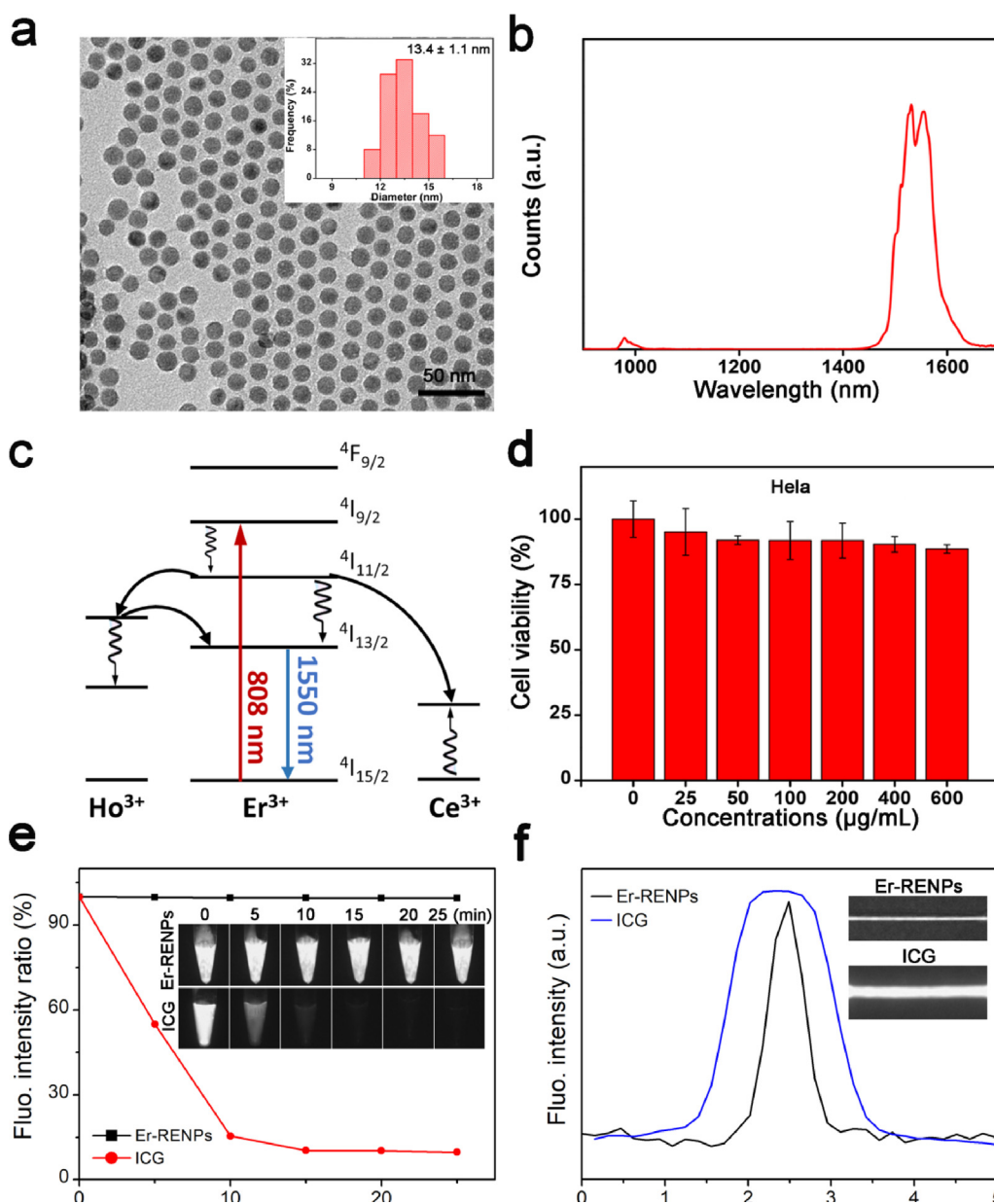


Fig. 1. (a) TEM image of Er-RENPs, and the particle size distribution histogram (insert), (b) photoluminescence spectrum of Er-RENPs under 808 nm excitation laser, (c) the energy-level diagrams depict the 1550 nm emission of Er-RENPs after excited by a 808 nm laser, (d) cell viability of HeLa cell line obtained through CCK-8 assay after incubated with different concentrations of Er-RENPs for 24 h, (e) photostability of Er-RENPs and ICG after exposed to 808 nm laser for 25 min at the power intensity of 1 W/cm^2 , together with (f) the phantom width of Er-RENPs and ICG capillary images taken with LP1250 and LP880 filters, respectively.

which is furtherly supported by the results of (DLS), showing only a sharp peak located at 18.2 nm (Fig. S1). In addition, the DLS peaks maintain the same in 72 h, indicating the excellent structural stability of the Er-RENPs. The result of fluorescence spectrum given in Fig. 1b reveals that the emission peak distributed at 1550 nm after 808 nm laser excitation, reflecting the Er-RENPs are appropriate for *in vivo* NIR-II fluorescence imaging. The quantum yield (QY) in NIR-II region of the Er-RENPs modified with polyethylene glycol (PEG) was 0.73% by taking IR-26 dye as a standard (Fig. S2), which is significantly higher than CNT (0.4%) [36], IR-26 (0.5%) [37], and comparable to the other RENPs reported previously [34]. The high QY is resulted from the rational design of the Er-RENPs (Fig. 1c). 808 nm laser excitation populated the $^4I_{9/2}$ energy level of Er^{3+} . Subsequently, the $Er^{3+} \ ^4I_{9/2} \rightarrow \ ^4I_{11/2}$, $^4I_{11/2} \rightarrow \ ^4I_{13/2}$ nonradiative transition occurred, populating the $^4I_{13/2}$ state of Er^{3+} . Meanwhile, the $Er^{3+} \ ^4I_{11/2}$ level transferred to Ho^{3+} and Ce^{3+} . Then the energy transferred to $Er^{3+} \ ^4I_{13/2}$ by nonradiative transition and nonradiative cross-relaxation, leading to a higher population of the $Er^{3+} \ ^4I_{13/2}$ state, which enhanced the 1550 nm downconversion NIR-II luminescence generation due to increasing radiative transition of $Er^{3+} \ ^4I_{13/2}$ returning to the ground state $Er^{3+} \ ^4I_{15/2}$. In addition, the core-shell structure and Er and Lu elements locating in core and shell can be determined by the EDX mapping displayed in Fig. S3. NaLuF₄ coating possesses good luminescence protection effect, because of its suppression on the non-radiative energy transition of luminescence center, which is in consistent with previous results [34,38,39]. Therefore, rational design endows the Er-RENPs good fluorescence property in NIR-II region, and further study confirms the deep tissue penetration of Er-RENPs (Fig. S4). Subsequently, the cytotoxicity evaluated by cell counting kit-8 (CCK-8) assay shows that the cell viabilities of both Hela and NIH 3T3 cell lines are remained higher than 80% (Figs. 1d and S5), even with Er^{3+} concentration as high as 600 $\mu\text{g}/\text{mL}$, demonstrating excellent biocompatibility of the Er-RENPs. To further explore the potential of Er-RENPs for *in vivo* bioimaging, the photobleaching experiment was performed, with clinically used fluorescence dye ICG (NIR-I, 835 nm) as a reference. As shown in Fig. 1e, distinct from the remarkable fluorescence quenching of ICG, Er-RENPs has almost no fluorescence attenuation after 25 min irradiation with 808 nm laser (1 W/cm^2), indicating the photostability of the Er-RENPs.

Moreover, the phantom width of Er-RENPs capillary image (about 1.0 mm) is significantly narrower than that of ICG (about 1.8 mm) (Fig. 1f), elucidating the superior fidelity of NIR-II emitted Er-RENPs over NIR-I emitted ICG. Therefore, the Er-RENPs may display lesions more accurately, and present more pathological details when it is utilized for *in vivo* bioimaging, outperforming clinically used ICG.

To explore the potential application of the Er-RENPs for tubal imaging, *in vivo* experiments were employed. Figs. 2b and S6 show the NIR-II imaging of normal fallopian tubes. The partial fallopian tube was lighted up just after 1 s injection of Er-RENPs. The lighted area of fallopian tube becomes larger, and sinuous outline of the fallopian tube becomes clearer with the lapse of time. At 45 s after the nanoprobe administration, the fluorescent signal filled the entire fallopian tube, which delineates the structures of fallopian tube (Fig. 2b), facilitating the diagnosis of tubal lesions. Additionally, we also tested the NIR-II imaging in slender fallopian tube with Er-RENPs serving as the fluorescence probe. As shown in Figs. 2c and S7, the lightened area in fallopian tube becomes larger over time, and the outline of the whole tubal can be observed until 180 s after Er-RENPs administration, taking much longer time than in the normal ones, which is attributed to the larger resistance the nanoprobe encountered when passes through the slender fallopian tube. These results indicate that NIR-II imaging has good performance in of normal and slender fallopian tubes, with the Er-RENPs serve as the fluorescence agent.

The excellent NIR-II imaging ability of the Er-RENPs in fallopian tube encouraged us to investigate their potential application for the diagnosis of the tubal diseases. As depicted in Fig. 3a, we prepared occlusive and stenotic tubal models by ligating fallopian tubes with surgical sutures. After the nanoprobe injected into occlusive or stenotic fallopian tubes, NIR-II imaging was recorded immediately. It can be observed that fluorescent signal diffused in the occlusive fallopian tube, and is blocked at the ligated site, making it easy to accurately identify the occluded lesion (Figs. 3b and S8). As for the stenotic fallopian tube, the fluorescent signal stalls at the ligated site for a short while, then breaks through the ligated site, and lights up the entire fallopian tube (Figs. 3c and S9). It is noteworthy that the signal at the ligated site is deficient, and about 2.8-fold weaker than that in front of the ligated

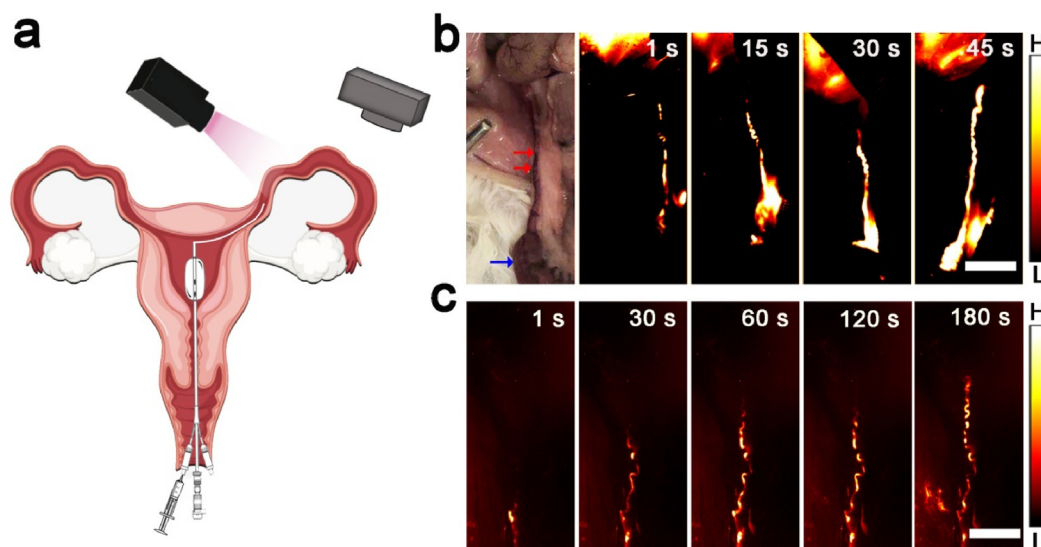


Fig. 2. (a) Schematic illustration of fallopian tube NIR-II imaging together with the Er-RENPs administration, (b) photographs of normal fallopian tube obtained by bright field imaging (fallopian tube, and uterus are marked with red, and blue arrows respectively), and NIR-II fluorescence imaging following 400 μL Er-RENPs (1 mg mL^{-1}) administration, (c) photographs of slender fallopian tube obtained by NIR-II imaging system (scale bar, 1 cm). (For interpretation of the references to colour in this figure legend, the reader is referred to the web version of this article.)

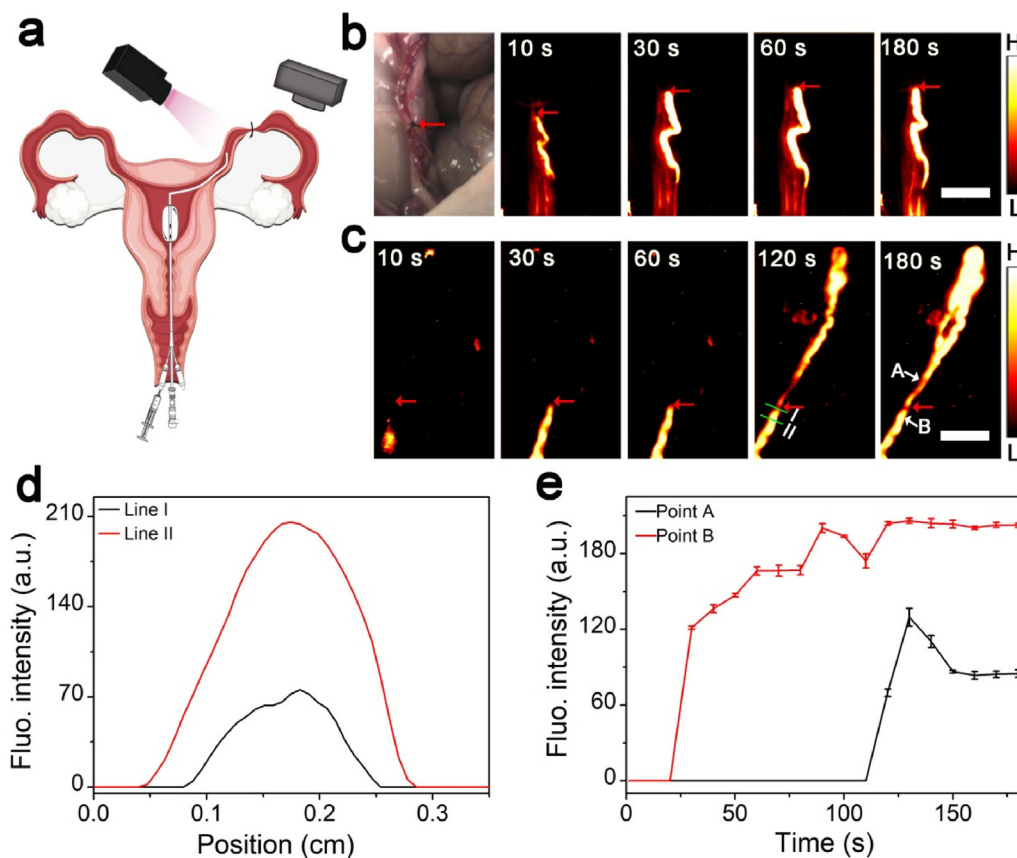


Fig. 3. (a) Schematic illustration of occlusive and stenotic fallopian tube models construction together with stenotic and occlusive tubal NIR-II imaging, together with (b) photographs of stenotic fallopian tube, (c) and occlusive fallopian tube obtained through NIR-II imaging system after Er-RENPs administration, (d) and the fluorescence intensity analysis based on the cross-sectional intensity profiles in (c), (e) as well as the time-dependent fluorescence intensity spectra of the selected points behind (point A in figure c) and in front of (point B in figure c) the ligated site (scare bar, 1 cm).

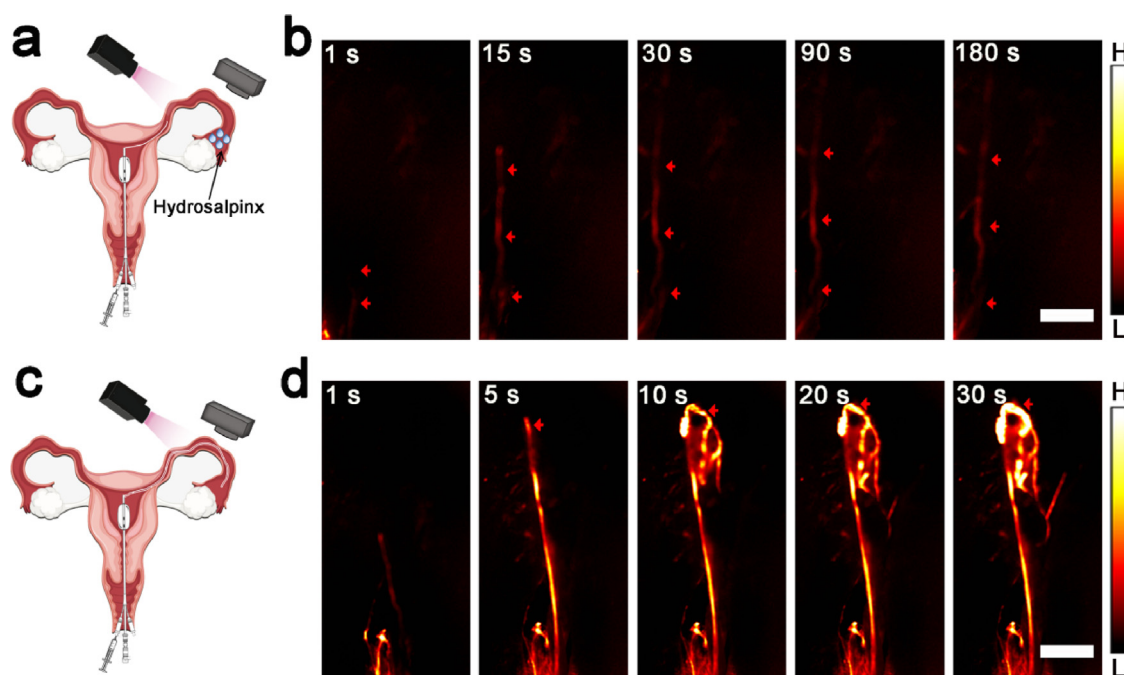


Fig. 4. (a) Schematic diagram of modeling and NIR-II imaging of hydrosalpinx, (b) photographs of hydrosalpinx tubal NIR-II imaging with Er-RENPs serving as fluorescence agent (fallopian tube marked with red arrows), (c) Schematic illustrating hydrosalpinx unclogging, and NIR-II imaging, (d) photographs of unclogged hydrosalpinx tubal NIR-II imaging obtained by NIR-II imaging system, red arrows denote tubal fimbria (scare bar, 1 cm). (For interpretation of the references to colour in this figure legend, the reader is referred to the web version of this article.)

site (Fig. 3d). Additionally, the fluorescence intensity behind the ligated site is much weaker than the counterpart in front of the ligated site, originating from less flux of fluorescence agent passing the ligated site (Fig. 3e), which makes it easy for doctors to diagnose the patency of the fallopian, and identify the stenotic site precisely, reflecting the considerable potential of the NIR-II imaging in the diagnosis of tubal diseases, especially the lesions identification, with the aid of the Er-RENPs nanoprobes.

We further explored the NIR-II imaging of fallopian tube with hydrosalpinx, a common infertility-causing tubal disease [40], with the help of the Er-RENPs. As shown in Fig. 4a, hydrosalpinx model was prepared, and then the Er-RENPs were administrated. Fallopian tube with hydrosalpinx can be faintly visualized with the NIR-II imaging system, which is attributed to the enormous pressure of fimbria (Figs. 4b and S10). In stark contrast, fallopian tube was rapidly lighted up, after the Er-RENPs injection and the swollen tubal fimbria can be clearly observed (marked with red arrows in Figs. 4d and S11) once the hydrosalpinx was unlogged via a stent (Fig. 4c). It was demonstrated that NIR-II imaging based on the Er-RENPs can not only utilized for the hydrosalpinx diagnosis, but also evaluating of the unlogging effect.

In addition, the process of the Er-RENPs excretion from fallopian tube, which may be associated with potential toxicity, is monitored. As shown in Figs. 5a and S12, diffuse fluorescence signal can be observed at the ovarian side, after the entire fallopian tube is lighted up. The area of diffuse signal becomes larger, accompanied by the dimming of the fluorescence signal in the fallopian tube with the lapse of time. The signal changes indicate that the injected Er-RENPs are mainly excreted into abdominal cavity through the opening of the ovary. The fallopian tube can be barely observed after 120 min demonstrating the successful expel of Er-RENPs. Furthermore, to figure out whether stenotic fallopian tube affects the excretion of the nanoprobes, we also explored the excretion process of the Er-RENPs in stenotic fallopian tube. Similarly, the Er-RENPs at the back of the ligated site can slowly be excreted into abdominal cavity through ovary, whereas the nanoprobes in front of the ligated site is expelled through uterus-vagina (Figs. 5b and S13). Most of the nanoprobes can be expelled from stenotic fallopian tube in 120 min.

Meanwhile, histological analysis of fallopian tubes, ovaries, uterus and the other major organs (liver, kidney, heart, spleen, and lung) was performed to evaluate *in vivo* biocompatibility of

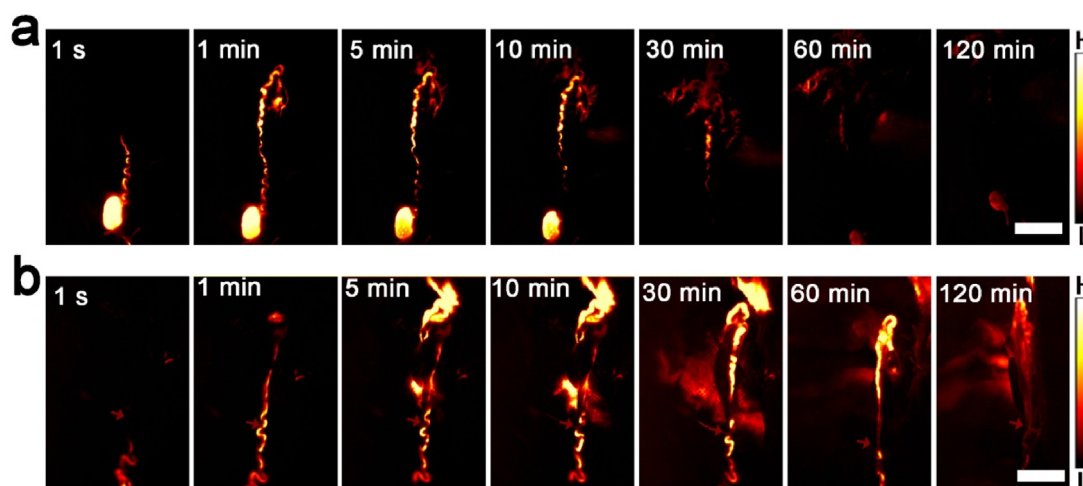


Fig. 5. The Er-RENPs excretion process from (a) normal, and (b) stenotic fallopian tubes investigated using NIR-II imaging after 400 μL Er-RENPs (1 mg mL^{-1}) administration, red arrows epitomize ligation site (scale bar, 1 cm). (For interpretation of the references to colour in this figure legend, the reader is referred to the web version of this article.)

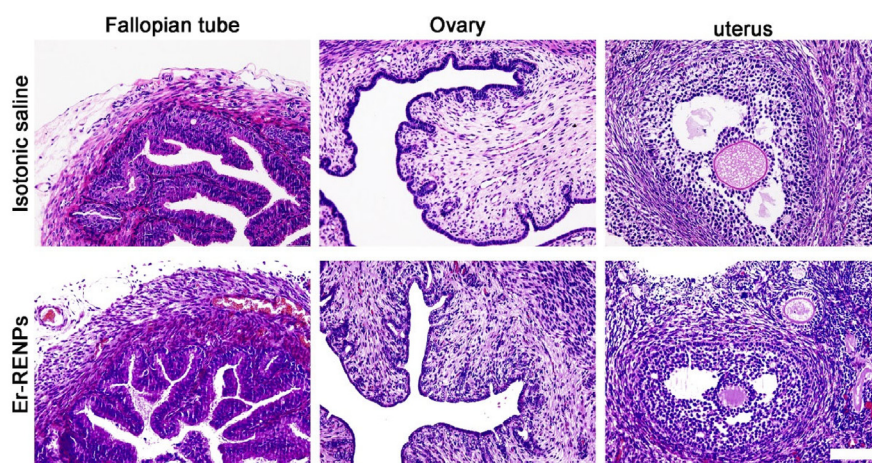


Fig. 6. Images of histologic section staining with H&E reflecting biocompatibility of the Er-RENPs to female rabbit's reproductive system (fallopian tubes, uteruses, and ovaries) after the Er-RENPs injection for 2 h (scale bar, 100 μm).

the Er-RENPs. From the photographs recording hematoxylin and eosin (H&E) staining displayed in Figs. 6 and S14, it can be observed that there is no significant difference between Er-RENPs administration group and control group (treated with isotonic saline), illustrating the outstanding biocompatibility, and the safety of the Er-RENPs for biomedical application. In addition, it is reported that rare earth nanoparticles (RENPs) are often retained in the liver and spleen for 1–2 weeks after administration [41], which may lead to potential long-term toxicity to liver and spleen. Thus, the histological analysis was employed at Day 10 after Er-RENPs administration. As shown in Fig. S15, no clear histological injury (such as edema and inflammation) of liver, spleen as well as the other major organs can be observed in both control and Er-RENPs groups, which may alleviate the concerns of long-term toxicity to liver and spleen.

4. Conclusions

In summary, a kind of the core-shell rare-earth Er-RENPs processing excellent NIR-II fluorescent capability and biocompatibility was synthesized by a simple one-pot reaction. The normal and slender fallopian tubes can be clearly visualized by NIR-II imaging system with the Er-RENPs serving as fluorescence probe. Moreover, the blockage lesions can be easily determined in stenotic and occlusive fallopian tubes. Furthermore, the Er-RENPs enable the successful diagnose of hydrosalpinx, and the efficacy can be assessed after the hydrosalpinx unclogged. Last but not least, most of the Er-RENPs can be expelled into abdominal cavity from fallopian tubes through the opening of ovary after 120 min of administration, exhibiting good biosafety for the reproductive system of female rabbits. Thus, NIR-II imaging has the potential to be developed as an alternative to HSG for tubal patency diagnosis, with the aid of Er-RENPs nanoprobe.

5. Credit author statement

G.D. and Z.W. contributed equally to this work. L.W., H.Z., M.G. designed the research. G.D., Z.W., J.Z., X.L. conducted the experiments. All authors analyzed and discussed on the results. G.D., Z.W., S.W., J.Z., and L.W. co-write the manuscript. L.W., H.Z., and M.G. edited the manuscript.

Data availability

The data and materials in the current study are available from the corresponding author on reasonable request.

Declaration of Competing Interest

The authors declare that they have no known competing financial interests or personal relationships that could have appeared to influence the work reported in this paper.

Acknowledgements

This work was supported by the National Natural Science Foundation of China (82172044, 22006109), the Medical Scientific Research Project of Jiangsu Provincial Health Commission (H2019086), the Project of State Key Laboratory of Radiation Medicine and Protection (GZK1201915).

Appendix A. Supplementary material

Supplementary data to this article can be found online at <https://doi.org/10.1016/j.matdes.2023.111726>.

References

- [1] R. Hunter, Have the Fallopian tubes a vital role in promoting fertility?, *Acta Obstet Gynecol. Scand.* 77 (1998) 475–486.
- [2] S. Das, L.G. Nardo, M.W. Seif, Proximal tubal disease: the place for tubal cannulation, *Reprod. Biomed. Online* 15 (2007) 383–388.
- [3] J.M. Goldberg, T. Falcone, M.P. Diamond, Current controversies in tubal disease, endometriosis, and pelvic adhesion, *Fertil. Steril.* 112 (2019) 417–425, <https://doi.org/10.1016/j.fertnstert.2019.06.021>.
- [4] Q. Wu, Y. Lin, J. Zhang, Y. Zhou, L. Chen, T. Lin, Preliminary hysteroscopic tubal hydrotubation improves fertility outcomes after laparoscopic salpingotomy for tubal ampullary pregnancy, *BMC Surg.* 22 (2022) 1–6.
- [5] W.H. Organization, Comparative trial of tubal insufflation, hysterosalpingography, and laparoscopy with dye hydrotubation for assessment of tubal patency, *Fertil. Steril.* 46 (1986) 1101–1107.
- [6] S. Shah, O. Towobola, M. Masihleho, Diagnosis of fallopian tube patency, *East Afr. Med. J.* 82 (2005).
- [7] F. Chenia, G. Hofmeyr, S. Moolla, P. Oratis, Sonographic hydrotubation using agitated saline: a new technique for improving fallopian tube visualization, *Br. J. Radiol.* 70 (1997) 833–836.
- [8] X. Liu, H. Cui, W. Chen, X. Xuan, X. Guo, Y. Hu, Diagnosis and treatment of fallopian tube obstruction: a literature review, *Int. J. Clin. Exp. Med.* 10 (2017) 15950–15959.
- [9] W.L. Simpson Jr, L.G. Beitia, J. Mester, Hysterosalpingography: a reemerging study, *Radiographics* 26 (2006) 419–431.
- [10] A. Chalazonitis, I. Tzovara, F. Laspas, P. Porfyridis, N. Ptohis, G. Tsimitselis, Hysterosalpingography: technique and applications, *Curr. Probl. Diagn. Radiol.* 38 (2009) 199–205.
- [11] J.L. Evers, J.A. Land, B.W. Mol, Evidence-based medicine for diagnostic questions, *Seminars in reproductive medicine*, Copyright© 2003 by Thieme Medical Publishers, Inc., 333 Seventh Avenue, New York, 2003, pp. 009–016.
- [12] P.L. Choyke, H. Kobayashi, Medical uses of fluorescence imaging: bringing disease to light, *IEEE J. Sel. Top. Quantum Electron.* 18 (2011) 1140–1146.
- [13] X. Tian, Z. Yang, G. Duan, A. Wu, Z. Gu, L. Zhang, C. Chen, Z. Chai, C. Ge, R. Zhou, Graphene oxide nanosheets retard cellular migration via disruption of actin cytoskeleton, *Small* 13 (2017) 1602133.
- [14] D. Huang, S. Lin, Q. Wang, Y. Zhang, C. Li, R. Ji, M. Wang, G. Chen, Q. Wang, An NIR-II fluorescence/dual bioluminescence multiplexed imaging for in vivo visualizing the location, survival, and differentiation of transplanted stem cells, *Adv. Funct. Mater.* 29 (2019) 1806546.
- [15] B. Li, M. Zhao, L. Feng, C. Dou, S. Ding, G. Zhou, L. Lu, H. Zhang, F. Chen, X. Li, Organic NIR-II molecule with long blood half-life for in vivo dynamic vascular imaging, *Nat. Commun.* 11 (2020) 1–11.
- [16] X. Song, W. Zhu, X. Ge, R. Li, S. Li, X. Chen, J. Song, J. Xie, X. Chen, H. Yang, A new class of NIR-II gold nanocluster-based protein biolabels for in vivo tumor-targeted imaging, *Angew. Chem. Int. Ed.* 60 (2021) 1306–1312.
- [17] S. Liu, C. Chen, Y. Li, H. Zhang, J. Liu, R. Wang, S.T. Wong, J.W. Lam, D. Ding, B.Z. Tang, Constitutional isomerization enables bright NIR-II AIEgen for brain-inflammation imaging, *Adv. Funct. Mater.* 30 (2020) 1908125.
- [18] X. Zhang, M. Zhao, L. Wen, M. Wu, Y. Yang, Y. Zhang, Y. Wu, J. Zhong, H. Shi, J. Zeng, Sequential SPECT and NIR-II imaging of tumor and sentinel lymph node metastasis for diagnosis and image-guided surgery, *Biomater. Sci.* 9 (2021) 3069–3075.
- [19] X. Zhang, X. Li, W. Shi, H. Ma, Sensitive imaging of tumors using a nitroreductase-activated fluorescence probe in the NIR-II window, *Chem. Commun.* 57 (2021) 8174–8177.
- [20] W. Xu, D. Wang, B.Z. Tang, NIR-II AIEgens: a win-win integration towards bioapplications, *Angew. Chem.* 133 (2021) 7552–7563.
- [21] H. Huang, Z. Sun, H. Yang, X. Yang, F. Wu, Y. Sun, C. Li, M. Tian, H. Zhang, Q. Wang, Precise examination of peripheral vascular disease for diabetics with a novel multiplexed NIR-II fluorescence imaging technology, *Nano Today* 43 (2022) 101378.
- [22] R. Tian, H. Ma, S. Zhu, J. Lau, R. Ma, Y. Liu, L. Lin, S. Chandra, S. Wang, X. Zhu, Multiplexed NIR-II probes for lymph node-invaded cancer detection and imaging-guided surgery, *Adv. Mater.* 32 (2020) 1907365.
- [23] C. Li, Y. Zhang, M. Wang, Y. Zhang, G. Chen, L. Li, D. Wu, Q. Wang, In vivo real-time visualization of tissue blood flow and angiogenesis using Ag2S quantum dots in the NIR-II window, *Biomaterials* 35 (2014) 393–400.
- [24] L. Bai, Z. Hu, T. Han, Y. Wang, J. Xu, G. Jiang, X. Feng, B. Sun, X. Liu, R. Tian, Super-stable cyanine@ albumin fluorophore for enhanced NIR-II bioimaging, *Theranostics* 12 (2022) 4536.
- [25] X. Fan, Q. Xia, Y. Zhang, Y. Li, Z. Feng, J. Zhou, J. Qi, B.Z. Tang, J. Qian, H. Lin, Aggregation-Induced Emission (AIE) nanoparticles-assisted NIR-II fluorescence imaging-guided diagnosis and surgery for Inflammatory Bowel Disease (IBD), *Adv. Healthc. Mater.* 10 (2021) 2101043.
- [26] Y. Yang, S. Wang, L. Lu, Q. Zhang, P. Yu, Y. Fan, F. Zhang, NIR-II chemiluminescence molecular sensor for in vivo high-contrast inflammation imaging, *Angew. Chem.* 132 (2020) 18538–18543.
- [27] S. Wang, L. Liu, Y. Fan, A.M. El-Toni, M.S. Alhoshan, D. Li, F. Zhang, In vivo high-resolution ratiometric fluorescence imaging of inflammation using NIR-II nanoprobes with 1550 nm emission, *Nano Lett.* 19 (2019) 2418–2427.
- [28] Z. Hu, C. Fang, B. Li, Z. Zhang, C. Cao, M. Cai, S. Su, X. Sun, X. Shi, C. Li, First-in-human liver-tumour surgery guided by multispectral fluorescence imaging in the visible and near-infrared-I/II windows, *Nat. Biomed. Eng.* 4 (2020) 259–271.

- [29] J.T. Robinson, G. Hong, Y. Liang, B. Zhang, O.K. Yaghi, H. Dai, In vivo fluorescence imaging in the second near-infrared window with long circulating carbon nanotubes capable of ultrahigh tumor uptake, *J. Am. Chem. Soc.* 134 (2012) 10664–10669.
- [30] G. Hong, J.T. Robinson, Y. Zhang, S. Diao, A.L. Antaris, Q. Wang, H. Dai, In vivo fluorescence imaging with Ag₂S quantum dots in the second near-infrared region, *Angew. Chem. Int. Ed.* 51 (2012) 9818–9821.
- [31] B. Dong, C. Li, G. Chen, Y. Zhang, Y. Zhang, M. Deng, Q. Wang, Facile synthesis of highly photoluminescent Ag₂Se quantum dots as a new fluorescent probe in the second near-infrared window for in vivo imaging, *Chem. Mater.* 25 (2013) 2503–2509.
- [32] S. Liu, Y. Li, R.T. Kwok, J.W. Lam, B.Z. Tang, Structural and process controls of AlEgens for NIR-II theranostics, *Chem. Sci.* 12 (2021) 3427–3436.
- [33] Y. Fan, P. Wang, Y. Lu, R. Wang, L. Zhou, X. Zheng, X. Li, J.A. Piper, F. Zhang, Lifetime-engineered NIR-II nanoparticles unlock multiplexed in vivo imaging, *Nat. Nanotechnol.* 13 (2018) 941–946.
- [34] Z. Wei, G. Duan, B. Huang, S. Qiu, D. Zhou, J. Zeng, J. Cui, C. Hu, X. Wang, L. Wen, Rapidly liver-clearable rare-earth core-shell nanoprobe for dual-modal breast cancer imaging in the second near-infrared window, *J. Nanobiotechnol.* 19 (2021) 1–14.
- [35] X. Wang, J. Zhuang, Q. Peng, Y. Li, A general strategy for nanocrystal synthesis, *Nature* 437 (2005) 121–124.
- [36] A.L. Antaris, H. Chen, K. Cheng, Y. Sun, G. Hong, C. Qu, S. Diao, Z. Deng, X. Hu, B. Zhang, A small-molecule dye for NIR-II imaging, *Nat. Mater.* 15 (2016) 235–242.
- [37] Y. Li, Z. Li, D. Hu, S. Wang, M. Zha, S.-B. Lu, Z. Sheng, K. Li, Targeted NIR-II emissive nanoprobe for tumor detection in mice and rabbits, *Chem. Commun.* 57 (2021) 6420–6423.
- [38] Z. Wang, P. Zhang, Q. Yuan, X. Xu, P. Lei, X. Liu, Y. Su, L. Dong, J. Feng, H. Zhang, Nd³⁺-sensitized NaLuF₄ luminescent nanoparticles for multimodal imaging and temperature sensing under 808 nm excitation, *Nanoscale* 7 (2015) 17861–17870.
- [39] Q. Li, X. Li, L. Zhang, J. Zuo, Y. Zhang, X. Liu, L. Tu, B. Xue, Y. Chang, X. Kong, An 800 nm driven NaErF₄@NaLuF₄ upconversion platform for multimodality imaging and photodynamic therapy, *Nanoscale* 10 (2018) 12356–12363.
- [40] O. Chanelles, G. Ducarme, C. Sifer, J.-N. Hugues, C. Touboul, C. Poncelet, Hydrosalpinx and infertility: what about conservative surgical management?, *Euro J. Obstet. Gynecol. Reprod. Biol.* 159 (2011) 122–126.
- [41] Y. Zhong, Z. Ma, F. Wang, X. Wang, Y. Yang, Y. Liu, X. Zhao, J. Li, H. Du, M. Zhang, In vivo molecular imaging for immunotherapy using ultra-bright near-infrared-IIb rare-earth nanoparticles, *Nat. Biotechnol.* 37 (2019) 1322–1331.